

Solution Structure of the IIA^{Chitobiose}-HPr complex of the *N,N'*-Diacetylchitobiose Branch of the *Escherichia coli* Phosphotransferase system. *

Young-Sang Jung†‡, Mengli Cai† and G. Marius Clore¶

From the Laboratory of Chemical Physics, NIDDK, National Institutes of Health, Bethesda, Maryland 20892

Running Title: Solution structure of the IIA^{Chb}-HPr complex

¶Address correspondence to: G. Marius Clore, Laboratory of Chemical Physics, Bldg 5, Rm. B1-30I, NIDDK, National Institutes of Health, Bethesda, MD 20892-0520. Tel: 301-496-0782; Fax: 301-496-0825; E-mail: mariusc@intr.niddk.nih.gov.

Key words: phosphoenolpyruvate:sugar phosphotransferase pathway / signal transduction / protein-protein interactions / phosphoryl transfer / NMR spectroscopy

Background: The bacterial phosphoryl transfer system (PTS) couples phosphoryl transfer to sugar transport.

Results: The structure of the IIA^{chitobiose}-HPr complex completes the structure elucidation of representative cytoplasmic complexes for all four sugar branches of the PTS.

Conclusion: Phosphoryl transfer occurs without any significant backbone conformational changes.

Significance: Recognition of multiple, structurally diverse partners is facilitated by complementary interaction surfaces and side chain conformational plasticity.

The solution structure of the complex of enzyme IIA of the *N,N'*-diacetylchitobiose (Chb) transporter with the histidine phosphocarrier protein HPr has been solved by NMR. The IIA^{Chb}-HPr complex completes the structure elucidation of representative cytoplasmic complexes for all four sugar branches of the bacterial phosphoryl transfer system (PTS). The active site His-89 of IIA^{Chb} was mutated to Glu to mimic the phosphorylated state. IIA^{Chb}(H89E) and HPr form a weak complex with a K_D of ~0.7 mM. The interacting binding surfaces, concave for IIA^{Chb} and convex for HPr, complement each other in terms of shape, residue type and charge distribution, with predominantly hydrophobic residues, interspersed by some uncharged polar residues, located centrally, and polar and charged residues at the periphery. The active site histidine of HPr, His15, is buried within the active site cleft of IIA^{Chb} formed at the interface of two adjacent subunits of the IIA^{Chb} trimer, thereby coming into close proximity with the active site residue, H89E, of IIA^{Chb}. A His89-P-His15 pentacoordinate phosphoryl transition state can readily be modeled without necessitating any significant conformational changes, thereby facilitating rapid phosphoryl transfer. Comparison of the IIA^{Chb}-HPr complex with the IIA^{Chb}-IIB^{Chb} complex, as well as with other cytoplasmic complexes of the

PTS, highlights a unifying mechanism for recognition of structurally diverse partners. This involves generating similar binding surfaces from entirely different underlying structural elements, large interaction surfaces coupled with extensive redundancy, and side chain conformational plasticity to optimize diverse sets of intermolecular interactions.

The phosphoenolpyruvate:sugar phosphotransferase system (PTS)¹ is a central bacterial signal transduction pathway in which phosphoryl transfer, via a series of bimolecular protein-protein complexes, is coupled to both sugar transport across the membrane and the regulation of many cellular processes, including catabolite repression (1-6). The first component of the PTS, enzyme I, is autophosphorylated by phosphoenolpyruvate and subsequently transfers the phosphoryl group to the histidine phosphocarrier protein (HPr). HPr then transfers the phosphoryl group to the A domain of the sugar specific enzymes II, which are divided into four structurally distinct families corresponding to the glucose, mannose, mannitol, and lactose/chitobiose branches of the PTS. All enzymes II have similar organizations comprising A and B cytoplasmic domains, and a membrane bound sugar transporter comprising the C domain, and sometimes a D domain as well. In some instances the domains

are expressed as a contiguous protein, in others as separate proteins. From IIA, the phosphoryl group is transferred to IIB, and finally onto the incoming sugar molecule bound to the transmembrane IIC domain. Despite the similar domain organization of the enzymes II, the A and B cytoplasmic domains from the different branches of the PTS bear no sequence similarity to one another, and with the exception of IIB^{Mtl} (7,8) and IIB^{Chb} (9-11), no similarity in either ternary or quaternary structures either.

Structures of the individual cytoplasmic components of the PTS have been solved by either NMR (7,8,10-20) or crystallography (9,21-35). Structures of the cytoplasmic protein-protein complexes of the PTS, however, have been intractable to crystallography, presumably due to their weak affinity making successful co-crystallization difficult. Weak binding, however, is not an impediment to NMR, and we have solved the solution structures of all the cytoplasmic binary protein complexes of the PTS (15,16,18,36-43) with the exception of the IIA^{Chb}-HPr complex. These complexes provide a wealth of information for understanding the unifying mechanism whereby a common interface, coupled with side chain conformational plasticity, can be used to recognize multiple, structurally dissimilar partners, and in addition, have yielded the first direct experimental evidence for the existence of highly transient, sparsely-populated encounter complexes (44-46).

In this paper we present the solution structure of the IIA^{Chb}-HPr complex, the remaining outstanding cytoplasmic complex of the PTS, thereby completing our long-term goal of solving all the cytoplasmic complexes of the PTS.

EXPERIMENTAL PROCEDURES

Protein Expression and Mutagenesis – Genes encoding IIA^{Chb*} (corresponding to a NΔ13/D92L mutant of wild-type IIA^{Chb}) (20) and HPr (39,47) were cloned into the pET-11 vector. H89E and H15D mutations of the active site histidines of IIA^{Chb*} and HPr, respectively, were introduced using the Quikchange mutagenesis kit (Stratagene, La Jolla, CA). (Residues of HPr are denoted in italics throughout). Both mutations were designed to mimic the charge effect of phosphorylation of the active site histidines.

The IIA^{Chb*}, IIA^{Chb*}(H89E), HPr, and HPr(H15D) plasmids were introduced into *E. coli* BL21(DE3) (Novagen) cells for protein expression and induced at an A₆₀₀ ~ 0.8 with 1 mM isopropyl-β-

d-thiogalactopyranoside at 37°C. Cells were grown in either Luria-Bertani medium or minimal medium (in either H₂O or D₂O) with ¹⁵NH₄Cl or ¹⁴NH₄Cl as the sole nitrogen source, and U-[¹³C/¹H], U-[¹²C/¹H], U-[¹³C/²H], or U-[¹²C/²H] glucose as the main carbon source. Because Leu, Val, Ile, Met, Gly, Try, Ser, Phe, and Ala residues are involved in the IIA^{Chb*}-HPr binding interface, selective amino acid labeling was also employed in the preparation of NMR samples. For ²H/¹³C/¹⁵N-(Ile/Leu/Val)-methyl-protonated (but otherwise fully deuterated) protein samples, 100 mg of α-[¹³C₅,3-²H₁] ketoisovalerate and 50 mg of α-[¹³C₄,3,3-²H₂] ketobutyrate (Cambridge Isotopes) were added to 1 liter of D₂O medium 1 h prior to induction (48). ²H/¹²C/¹⁴N-(Ile/Gly/Phe-protonated)-IIA^{Chb*}(H89E), ²H/¹²C/¹⁴N-(Leu/Met/Tyr-protonated)-IIA^{Chb*}(H89E), and ²H/¹²C/¹⁴N-(Val/Ala/His-protonated)-IIA^{Chb*}(H89E) samples were prepared by supplementing 1 liter of D₂O medium with 300 mg of Ile/Gly/Phe/Leu/Met/Tyr/Val/Ala/His (Sigma Aldrich) at natural isotopic abundance 1 h prior to induction. Cells were grown an additional 7 h after induction. Cells expressing IIA^{Chb*}(H89E) or HPr were harvested by centrifugation at 15,900 × g for 25 min.

IIA^{Chb*} and IIA^{Chb*}(H89E), and HPr and HPr(H15D) were purified as described previously in refs (43) and (39), respectively.

NMR Data Collection and Analysis—All NMR samples were prepared in a buffer of 20 mM sodium phosphate, pH 7.4, 0.2 mM sodium azide, and either 90% H₂O/10% D₂O or 99.99% D₂O. IIA^{Chb*} is a symmetric trimer with three equivalent binding sites for HPr. As in the case of the IIA^{Chb*}(H89E)-IIB^{Chb}(C10S) complex (43), a 1:1 mixture of IIA^{Chb*}(H89E) trimer to HPr monomer was employed to achieve optimal linewidths for NMR spectroscopy. NMR spectra were recorded at 20 and 35°C on Bruker DMX500, DMX600, DRX600, DRX800, and DRX900 spectrometers equipped with z-shielded gradient triple resonance cryoprobes. Spectra were processed with the NMRPipe package (49) and analyzed using the programs PIPP (50) and XIPP (Garrett, D.S. and Clore, G.M., unpublished). Sequential and side chain assignments of IIA^{Chb*}(H89E) and HPr were derived from the following three-dimensional double and triple resonance through-bond correlation experiments (51,52): HNCA, HN(CO)CA, HNCACB, CBCA-(CO)HN, HAHN, HNCA-TROSY, HN(CO)CA-TROSY, HNCB-TROSY, HN(CO)CB-TROSY, C(CCO)NH, H(CCO)NH, and HCCH-TOCSY. Three-dimensional ¹⁵N-separated, ¹³C-separated, and ¹³C/¹³C-separated nuclear Overhauser enhancement

(NOE) experiments were used to facilitate side chain assignments (51).

Intermolecular NOEs were observed on the IIA^{Chb*}(H89E)-HPr complex in D₂O buffer using three-dimensional ¹²C-filtered(F₁)/¹³C-separated(F₂) or ¹³C-separated(F₂)/¹²C-filtered(F₃) NOE experiments, and in H₂O buffer using two-dimensional ¹⁵N-separated/¹³C-edited and ¹³C-separated/¹⁵N-edited NOE experiments (53,54). Nine different combinations of isotope-labeled complexes were used for analysis of intermolecular NOEs (Table 1).

Structure Calculations—NOE-derived interproton distance restraints were classified into loose approximate distance ranges of 1.8–2.7, 1.8–3.5, 1.8–5.0, and 1.8–6.0 Å corresponding to strong, medium, weak, and very weak NOE cross-peak intensities, respectively (55). An empirical correction of 0.5 Å was added to the upper distance bounds of distance restraints involving methyl groups to account for the higher apparent intensity of methyl resonances (56), and NOEs involving non-stereospecifically assigned methyl, methylene, and aromatic protons were represented by a $(\sum r^{-6})^{-1/6}$ sum (57). Backbone torsion angle restraints for the active site region (residues 13–17) of HPr were derived from backbone ¹H/¹⁵N/¹³C chemical shifts using the program TALOS+ (58) and used in the calculations of the phosphoryl transition state. The current experiments yielded interproton distance restraints and interfacial side chain torsion angle restraints.

Structures were calculated using conjoined rigid body/torsion angle-simulated annealing (59,60) with the program Xplor-NIH (61). The minimized target function comprises NOE derived interproton distance restraints, torsion angle restraints, RDC restraints, ¹³Cα/¹³Cβ chemical shift restraints, a quartic van der Waals repulsion term for the non-bonded contacts, a multidimensional torsion angle data base potential of mean force (62), and a gyration volume potential to ensure optimal packing (63). Structure figures were generated using the programs VMD-XPLOR (64) and GRASP (65). Reweighted atomic probability density maps were calculated as described previously (66). The atomic coordinates and NMR experimental restraints (accession codes 2lrk and 2lrl for the unphosphorylated and phosphoryl transition state complexes, respectively) have been deposited in the Protein Data Bank, Research Collaboratory for Structural Bioinformatics, Rutgers University, New Brunswick, NJ.

RESULTS AND DISCUSSION

Equilibrium binding of IIA^{Chb*}(H89E) and HPr — At concentrations used in NMR experiments, wild type IIA^{Chb} is highly prone to non-specific aggregation promoted by the presence of a disordered 13-residue N-terminal tail and divalent cations required to neutralize and coordinate three symmetry-related, buried aspartate side chains (Asp92) located at the center of the trimer interface (20). As in previous work (20,43), we therefore made use of the IIA^{Chb*} construct throughout the current study. IIA^{Chb*} forms a stable monodisperse trimer, and comprises a deletion of the disordered 13-residue N-terminal tail and mutation of the buried Asp92 to Leu (20). Leu and Asp have similarly branched side chains, and the methyl groups of the three Leu92 side chains, one from each subunit, substitute well-packed hydrophobic methyl-methyl interactions at the trimer interface in place of the role fulfilled by the metal cation. These mutations do not affect phosphoryl transfer activity.

The interaction between IIA^{Chb*} and HPr was assessed by monitoring ¹H_N/¹⁵N chemical shift perturbations of ¹⁵N-labeled HPr upon addition of unlabeled IIA^{Chb*} (Fig. 1). Studies were carried out with HPr, IIA^{Chb*}, IIA^{Chb*}(H89E) and HPr(H15D). (Note that throughout the text, residues of HPr are printed in italics to distinguish them from residues of IIA^{Chb*}). The latter two mutations are designed to mimic the charge effects of phosphorylation of the active site histidines at the Nε2 (H89E) and Nδ1 (H15D) positions. At pH 7.4 and 20°C we could not detect any significant chemical shift perturbations upon addition of IIA^{Chb*} to either HPr or HPr(H15D) at the concentrations employed (up to ~1.2 mM in subunits of IIA^{Chb*} with ~0.4 mM HPr). However, measurable chemical shift perturbations were obtained upon addition of IIA^{Chb*}(H89E) to HPr yielding a *K_D* of 0.7±0.1 mM (Fig.1). Therefore all structural studies were carried out with the IIA^{Chb*}(H89E) phosphomimetic mutant.

Structure determination — The IIA^{Chb*}-HPr complex is in fast exchange on the chemical shift time scale (i.e. only a single set of population weighted average resonances are observed). The ¹H_N/¹⁵N chemical shift perturbations upon complex formation are small indicative of no significant change in backbone conformation (within the limits of the NMR method). The ¹H_N/¹⁵N chemical shift perturbations span residues 18–34 and 53–102 of IIA^{Chb*}, and residues 8–24, 52–53, 61–62, 80 and 85 of HPr, thereby providing an approximate delineation of the interaction surfaces.

Given that three molecules of HPr can bind to the $\text{IIA}^{\text{Chb}^*}$ symmetric dimer and binding is weak, all NMR experiments were carried on samples comprising 1 mM $\text{IIA}^{\text{Chb}^*}$ (in trimer) and 1 mM HPr. Under these conditions, there is 24% free HPr and 42%, 29% and 5%, singly, doubly and triply bound HPr; and 42% free $\text{IIA}^{\text{Chb}^*}$, and 42, 14 and 2% $\text{IIA}^{\text{Chb}^*}$ with one, two and three HPr molecules bound. Given molecular weights of ~ 34 and 9.5 kDa for free $\text{IIA}^{\text{Chb}^*}$ and HPr, respectively, the population weighted average masses of $\text{IIA}^{\text{Chb}^*}$ and HPr, which determine the linewidths in the NMR experiments, are ~ 40 kDa each. Note that the existence of multiple bound states, as well as the presence of a significant fraction of free proteins, precludes the use of residual dipolar couplings for determining the relative orientation of the two proteins in the complex, since the apparent alignment tensor can no longer be deconvoluted into individual alignment tensors for each component in the system (43).

The structure of the $\text{IIA}^{\text{Chb}^*}$ -HPr complex was largely based on intermolecular NOE data derived from 3D ^{12}C -filtered/ ^{13}C -separated 3D NOE experiments in which NOEs are exclusively observed between protons attached to ^{12}C and protons attached to ^{13}C . An array of different combinations of isotopically labeled samples, comprising both uniform and residue-specific labeling (Table 1), was employed to remove any ambiguities in assignment of intermolecular NOEs. An example of the quality of the intermolecular data is provided in Fig. 2.

The calculational strategy used to determine the structure of the complex made use of conjoined rigid body/torsion angle dynamics simulated annealing (60). In this instance, the backbone and non-interfacial side chains of the 2.0 \AA resolution X-ray coordinates of free HPr (30) were treated as a rigid body with rotational and translational degrees of freedom, while interfacial side chains were given torsional degrees of freedom. The only coordinates of free $\text{IIA}^{\text{Chb}^*}$ available are NMR coordinates (20) which are inherently less accurate than X-ray coordinates (especially in terms of translation and packing). Thus for $\text{IIA}^{\text{Chb}^*}$ full torsional, rotational and translational degrees of freedom were allowed with the coordinates restrained by the experimental NMR restraints (NOEs, torsion angles, dipolar couplings) obtained for free $\text{IIA}^{\text{Chb}^*}$ (20). This approach, rather than using the restrained regularized mean coordinates of free $\text{IIA}^{\text{Chb}^*}$ (20) as a rigid body, was employed since the interface of both partners is largely helical and therefore structurally rigid, the active site residue (H89E) is located within a deep cleft at the interface of adjacent subunits, and

therefore small errors in the backbone coordinates of the free NMR structure of $\text{IIA}^{\text{Chb}^*}$ can readily propagate and distort the docking of HPr onto $\text{IIA}^{\text{Chb}^*}$. The backbone coordinate shifts relative to the free $\text{IIA}^{\text{Chb}^*}$ coordinates, however, are small ($< 1 \text{ \AA}$) and well within the uncertainties of the NMR coordinates. In the case of the $\text{IIA}^{\text{Chb}^*}$ - IIB^{Chb} complex, on the other hand, the IIB^{Chb} interaction site comprises a loop so that uncertainties in the $\text{IIA}^{\text{Chb}^*}$ coordinates could be assimilated by simply giving the backbone of the active site loop of IIB^{Chb} torsional degrees of freedom, while treating the remaining backbone of IIB^{Chb} as well as the backbone of $\text{IIA}^{\text{Chb}^*}$ (excluding the disordered loop from residues 75-84) as rigid bodies (43).

As in the case of the weak $\text{IIA}^{\text{Chb}^*}$ - IIB^{Chb} complex, a heuristic approach was employed for interfacial side chains since the samples comprise a mixture of free and bound states (43). Thus, the interfacial side chains were given torsion angle degrees of freedom within the χ_1 and where appropriate χ_2 rotamers of the free structures, unless contradicted by the intermolecular NOE data.

A summary of the structural statistics is provided in Table 2, a best fit superposition of the final ensemble of 100 simulated annealing structures of the complex is displayed in Fig. 3A, and a reweighted atomic probability density map for some interfacial side chains is shown in Fig. 3B.

The overall structure of the $\text{IIA}^{\text{Chb}^}$ -HPr complex* — A ribbon diagram of the overall complex showing two and three molecules of HPr bound per trimer is displayed in Fig. 3B. Each HPr molecule interacts with two adjacent subunits of $\text{IIA}^{\text{Chb}^*}$: specifically subunits A and C, C and B, and B and A, where the first subunit in each pair contributes the active site residue at position 89. For the purposes of describing intermolecular contacts between HPr and $\text{IIA}^{\text{Chb}^*}$, we will restrict ourselves to the interaction surface formed at the interface of the A and C subunits of $\text{IIA}^{\text{Chb}^*}$.

Each subunit of $\text{IIA}^{\text{Chb}^*}$ comprises 3 helices in an up, down, up topology comprising residues 17-43 (helix 1), 47-74 (helix 2) and 85-114 (helix 3) (20). HPr has three helices formed by residues 16-28 (helix 1), 47-52 (helix 2) and 70-83 (helix 3), as well as a four-stranded antiparallel β -sheet (30). The active site histidine at position 89, as well as His93, of the A subunit of $\text{IIA}^{\text{Chb}^*}$ is located deep within a cleft formed at the interface of subunits A and C (Figs. 3B and 4A), while the active site His15 of HPr is exposed at the tip of a convex protrusion on the surface of HPr (Figs. 3B and 4B). The predominant intermolecular contacts between HPr and $\text{IIA}^{\text{Chb}^*}$

involve helices. The N-terminal halves of helices 1 (residues 16-27) and 2 (residues 347-348) of HPr interact with the N-terminal half of helix 1 (residues 18-33) and 3 (residues 89 and 93) of subunit A of IIA^{Chb*}; while the loop preceding helix 1 (residues 11-15), helix 2 (residues 47-53) and a stretch of extended strand (residues 55-57) of HPr interact with the C-terminal half of helix 2 (residues 58-73), the loop connecting helices 2 and 3 (residues 76-82), and the middle half of helix 3 (residues 91-98) of the C subunit of IIA^{Chb*}.

The total accessible surface area buried upon complex formation is $\sim 1580 \text{ \AA}^2$, comprising $\sim 350 \text{ \AA}^2$ and $\sim 450 \text{ \AA}^2$ for subunits A and C, respectively, of IIA^{Chb*}, and $\sim 780 \text{ \AA}^2$ for HPr (subdivided into ~ 350 and $\sim 430 \text{ \AA}^2$ for contacts with the A and C subunits of IIA^{Chb*}, respectively). The binding site on IIA^{Chb*} for both subunits A and C, comprises $\sim 45\%$ hydrophobic residues, with the remainder equally divided between polar and charged residues (Fig. 4A); for HPr, the portion of the binding surface that interacts with the A subunit of IIA^{Chb*} is $\sim 40\%$ hydrophobic, with the remainder equally divided between polar and charged residues (Fig. 4B, left half), while the portion of the HPr binding surface that interacts with the C subunit of IIA^{Chb*} is composed of $\sim 55\%$ hydrophobic and $\sim 45\%$ uncharged polar residues (Fig. 4B, right half). As in the other complexes of the PTS (15,16,36-40,43), the central portions of the interaction surfaces are largely, but not exclusively, hydrophobic, interspersed by uncharged polar residues, while the outer edges are predominantly charged or polar (Fig. 4).

Detailed views of the side chain interactions between HPr and the A and C subunits of IIA^{Chb*} are shown in Figs. 5A and B, respectively, together with a schematic summary of the intermolecular contacts in Fig. 5C. In contrast, to EIN, IIA^{Glc}, IIA^{Mtl} and IIA^{Man}, where the charged residues in the binding site for HPr are largely negative, with very few positively charged residues (36-39), the binding surface on IIA^{Chb*} (Fig. 4A) contains an equal number of positively and negatively charged residues (three of each), of which two negative (Glu19 and Glu73) and two positive (Arg58 and Lys62) residues participate in intermolecular electrostatic interactions (Fig. 5). Indeed there are a quite number of potential hydrogen bonding, salt bridge and longer range electrostatic interactions that serve to orient HPr and IIA^{Chb*} correctly.

Thus, at the interface between HPr and the A subunit of IIA^{Chb*}, the hydroxyl group of Thr16 forms a hydrogen bond with the Ne2 atom of H93^A;

the guanidino group of Arg17 forms potential salt bridges with the hydroxyl group of Ser33^A and the side chain carbonyl of Gln30^A, with the orientation of the side chain of Arg17 further stabilized by an intramolecular interaction between its guanidino group and the side chain carbonyl of Gln21; and Lys24 and Lys27 form potential salt bridge and longer range electrostatic interactions with the carboxylate of Glu19^A (Fig. 5A). In addition, the carboxylate of H89E^A is sufficiently close ($< 5 \text{ \AA}$) to the hydroxyl group of Thr16 to allow for an electrostatic interaction which may explain why the IIA^{Chb*}(H89E)-HPr complex is of higher affinity than either the IIA^{Chb*}-HPr or IIA^{Chb*}(H15D) complexes.

At the interface of HPr and the C subunit of IIA^{Chb*}, the side chain carbonyl of Gln57 has electrostatic interactions with the guanidino group of Arg58^C and the side chain amide group of Asn62^C; the side chain amide group of Asn12 forms a potential hydrogen bond with the S δ atom of Met98^C; the backbone amide of Leu53 donates a potential hydrogen bond to the carboxylate of Glu73^C; and the carboxamide group of Gln51 forms potential hydrogen bonds with the carboxylate of Glu73^C and the side chain amino group of Lys82^C (Fig. 5B).

Given that the interaction surfaces of HPr and IIA^{Chb*} are complementary both in terms of shape and distribution of residue type, it is likely that many of the above intermolecular electrostatic interactions are rather weak and transient, thereby accounting for the high equilibrium dissociation constant ($K_D \sim 0.7 \text{ mM}$; cf. Fig. 1) for the complex.

The phosphoryl transition state — It is known from isotope labeling experiments that the phosphoryl transition state in complexes of the PTS comprises a pentacoordinate phosphoryl group in a trigonal bipyramidal geometry, with donor and acceptor atoms at apical positions and the oxygen atoms of the phosphoryl group lying in an equatorial plane (67,68). The His89^A(Ne2)-P and His15(N δ 1)-P distances can lie anywhere between 1.8 and 3.5 \AA corresponding to pure associative and pure dissociative transition states, respectively, and the phosphorus atom lies in the plane of the imidazole group of both active site histidines.

To model the transition state, we therefore carried out conjoined rigid body/torsion angle simulated annealing calculations using exactly the same protocol and experimental restraints as those used for the unphosphorylated complex but with the addition of covalent geometry restraints for the pentacoordinate phosphoryl group and the introduction of backbone torsional degrees of

freedom for residues 13–17 of HPr encompassing the active site. The overall backbone rms shift between the restrained regularized mean structures of the transition state and unphosphorylated complexes is 0.5 Å overall, and 0.3 Å for the interface (Fig. 6B), which is well within the errors of the NMR coordinates. In addition, there are only minor perturbations in side chain positions (Fig. 6B). Thus, one can conclude that the transition state can be readily accommodated without any significant perturbation in backbone conformation. Further, agreement with the experimental restraints and indicators of structural quality are unaffected by the introduction of the phosphoryl transition state (Table 1).

The phosphoryl group in the transition state is hydrogen bonded to the hydroxyl group of *Thr16* of HPr, the He2 atom of *His93^A* of subunit A of *IIA^{Chb*}* and the carboxamide group of *Gln91^C* of subunit C of *IIA^{Chb*}* (Fig. 6A). As in other PTS complexes, the phosphoryl group is surrounded by a cluster of hydrophobic groups: *Leu47* and *Phe48* of HPr; *Val21^A*, *Ile25^A*, *Val86^A* and *Leu92^A* of the A subunit of *IIA^{Chb*}*; and *Ile72^C*, *Val83^C* and *Met95^C*, as well as the aliphatic portion of the side chain of *Lys82^C*, of the C subunit of *IIA^{Chb*}*.

Comparison with the IIA^{Chb}-IIB^{Chb} complex* — HPr (30) and *IIB^{Chb}* (9–11) share no similarity in either overall structure or local structure surrounding the active site residue, *His15* in the case of HPr, and *Cys11* for *IIB^{Chb}*. Yet both proteins bind to highly overlapping binding sites on *IIA^{Chb*}* (this paper and (43)). The interaction surfaces share 10 residues in common for subunit A and 9 for subunit C. The residues that are not shared by the two interaction surfaces are located at the peripheries of the binding sites. In the view shown in Fig. 4, the binding surface for HPr extends slightly upwards to include *Ser33^A* of subunit A and *Arg58^C*, *Asn62^C* and *Met98^C* of subunit C, while the binding surface for *IIB^{Chb}* extends slightly downwards to include *Glu15^A* of subunit A, and *Gly74^C* and *Gly77^C* of subunit C (43). These small differences can be readily appreciated by the superposition of the two complexes shown in Fig. 7, and probably reflect two factors: first, the slightly larger size of the binding site on *IIB^{Chb}* which comprises 29 residues versus 19 for HPr; and second the slightly more peripheral location of *His15* relative to the interaction surface compared to *Cys11* of *IIB^{Chb}*.

While small, the above differences nicely illustrate the concept of redundancy in a system in which one partner, *IIA^{Chb*}*, recognizes multiple partners, while making use of the same active site residue (*His89^A*)

to effect phosphoryl transfer. Thus, the four additional residues at the top edge of the *IIA^{Chb*}* binding surface for HPr that are not used in the interaction with *IIB^{Chb}*, namely *Ser33^A*, *Arg58^C*, *Asn62^C* and *Met98^C* (Fig. 4A), are all involved in potential hydrogen bonding and electrostatic interactions with HPr (Figs. 5A and B) that contribute to correctly orienting HPr relative to *IIA^{Chb*}*. The same is true of *Glu15^A*, located at the bottom edge of the *IIA^{Chb*}* binding surface for *IIB^{Chb}* but absent from the interaction with HPr, which forms a salt bridge with *Lys86* of *IIB^{Chb}* (43).

At the same time, side chain conformational plasticity, allows side chains to participate in similar interactions (cf. Fig. 5 of this paper and Fig. 4 of (43)). For example, *Gln30^A* forms a hydrogen bond with *Arg17* of HPr and *Tyr62* of *IIB^{Chb}*, both located in rather similar positions relative to their respective active site residues. Likewise, *Glu19^A* is involved in a potential salt bridge with *Lys27* of HPr and a potential electrostatic interaction with the hydroxyl group of *Ser33* of *IIB^{Chb}*. Finally, *Glu73^C* is hydrogen bonded to both the backbone amide of *Leu53* and the side chain amide of *Gln51* of HPr, and to the side chain guanidino group of *Arg24* of *IIB^{Chb}*.

As a final example, the interaction of *Met22^A* with *Phe48* of HPr (Fig. 5A) is very similar to that with *Tyr84* of *IIB^{Chb}*, except that the hydrophobic contacts between these two pairs of residues is supplemented by a potential hydrogen bond between the Sδ atom of *M22^A* and the hydroxyl group of *Tyr84*.

Concluding Remarks — The structure of the *IIA^{Chb*}*-HPr complex in the present paper completes the structure elucidation of representative soluble complexes for all four sugar branches of the PTS (15,16,18,36–40,43). This collection of structures provides a paradigm of protein recognition in signal transduction pathways that allows for multiple recognition partners, transient interactions and specificity.

Although the structures of the *IIA* components of the four sugar branches bear no sequence or structural similarity to one another, their recognition surfaces for HPr are remarkably similar in shape and residue composition. Moreover, each enzyme *IIA* makes use of highly overlapping surfaces to recognize both its upstream partner HPr and its downstream partner, enzyme *IIB* (This paper and (15,16,37–40,43)).

The ability to recognize multiple different partners relies on a number of design features. First, similar surfaces are constructed from completely different underlying structural elements. Thus, the shape of the binding surfaces on HPr and the four classes of

enzymes IIB are convex in shape and similar in size. Likewise, all four classes of enzymes IIA have a concave binding surface of similar size. Second, all the surfaces generally share similar features comprising predominantly hydrophobic residues, interspersed by uncharged polar residues, at the center of the interface surrounded by polar and charged residues at the periphery. Third, the interactions surfaces are all large (600-1000 Å²), thereby allowing considerable redundancy in the intermolecular interactions that have to be formed to achieve appropriate docking and orientation of the phosphoryl transfer complexes. A corollary to large surfaces and redundancy of specific intermolecular interactions is that all the complexes are transient and weak ranging from K_D values of ~10 μM to the millimolar range (This paper and (15,16,36-40,42,43)). Fourth, conformational plasticity of amino acids with long side chains (such as Arg, Lys and Glu) permit similar types of intermolecular interactions to occur across complexes involving one shared partner. Finally, although HPr uses the same binding surface to recognize enzyme I and all four classes of enzyme IIA, and the binding surfaces on the enzymes IIA used to interact with HPr and the corresponding enzymes IIB are highly overlapping, the absence of any detectable interaction between enzyme I and any of the enzymes IIB arises through

electrostatic selection. The binding surface on HPr contains no negative charges, and the charged residues on the binding surface of enzyme I are predominantly negative. In contrast, the binding surfaces on enzymes IIA and IIB comprise a mix of positively and negatively charged residues that largely complement one another. Thus these charged residues are either involved in intermolecular salt bridges, hydrogen-bonding interactions, or participate in van der Waals contacts. Intermolecular electrostatic repulsion, however, between like-charged residues is avoided. The positively charged residues located in the binding surface of the enzymes IIA are accommodated by the binding surface of HPr, either by making use of their long side chains in hydrophobic contacts, or by electrostatic interactions with polar groups (e.g. in the case of the IIA^{Chb*}-HPr complex, Arg58^C and Lys82^C of subunit C of IIA^{Chb*} interact with the side chain carbonyls of Gln57 and Gln51 of HPr, respectively).

Acknowledgments — We thank Dan Garrett and Dusty Baber for software and instrumental support, respectively. This paper is dedicated to the memory of Saul Roseman who discovered the bacterial phosphotransfer system.

REFERENCES

1. Kundig, W., Ghosh, S., and Roseman, S. (1964) Phosphate bound to histidine in a protein as an intermediate in a novel phospho-transferase system. *Proc. Natl. Acad. Sci. U. S. A.* **52**, 1067-1074
2. Meadow, N. D., Fox, D. K., and Roseman, S. (1990) The bacterial phosphoenolpyruvate: glucose phosphotransferase system. *Annu. Rev. Biochem.* **59**, 497-542
3. Postma, P. W., Lengeler, J. W., and Jacobson, G. R. (1993) Phosphoenolpyruvate:carbohydrate phosphotransferase systems of bacteria. *Microbiol. Rev.* **57**, 543-594
4. Robillard, G. T., and Broos, J. (1999) Structure/function studies on the bacterial carbohydrate transporters, enzymes II, of the phosphoenolpyruvate-dependent phosphotransferase system. *Biochim. Biophys. Acta* **1422**, 73-104
5. Siebold, C., Flukiger, K., Beutler, R., and Erni, B. (2001) Carbohydrate transporters of the bacterial phosphoenolpyruvate: sugar phosphotransferase system (PTS). *FEBS Lett.* **504**, 104-111
6. Deutscher, J., Francke, C., and Postma, P. W. (2006) How phosphotransferase system-related protein phosphorylation regulates carbohydrate metabolism in bacteria. *Microbiol. Mol. Biol. Rev.* **70**, 939-1031
7. Legler, P. M., Cai, M., Peterkofsky, A., and Clore, G. M. (2004) Three-dimensional solution structure of the cytoplasmic B domain of the mannitol transporter II^{mannitol} of the *Escherichia coli* phosphotransferase system. *J. Biol. Chem.* **279**, 39115-39121
8. Suh, J. Y., Tang, C., Cai, M., and Clore, G. M. (2005) Visualization of the phosphorylated active site loop of the cytoplasmic B domain of the mannitol transporter II^{mannitol} of the *Escherichia coli* phosphotransferase system by NMR spectroscopy and residual dipolar couplings. *J. Mol. Biol.* **353**, 1129-1136
9. van Montfort, R. L., Pijning, T., Kalk, K. H., Reizer, J., Saier, M. H., Jr., Thunnissen, M. M., Robillard, G. T., and Dijkstra, B. W. (1997) The structure of an energy-coupling protein from bacteria, IIB^{cellobiose}, reveals similarity to eukaryotic protein tyrosine phosphatases. *Structure* **5**, 217-225

10. Ab, E., Schuurman-Wolters, G., Reizer, J., Saier, M. H., Dijkstra, K., Scheek, R. M., and Robillard, G. T. (1997) The NMR side-chain assignments and solution structure of enzyme IIB^{cellobiose} of the phosphoenolpyruvate-dependent phosphotransferase system of *Escherichia coli*. *Protein Sci.* **6**, 304-314
11. Ab, E., Schuurman-Wolters, G. K., Nijlant, D., Dijkstra, K., Saier, M. H., Robillard, G. T., and Scheek, R. M. (2001) NMR structure of cysteinyl-phosphorylated enzyme IIB of the N,N'-diacetylchitobiose-specific phosphoenolpyruvate-dependent phosphotransferase system of *Escherichia coli*. *J. Mol. Biol.* **308**, 993-1009
12. Kalbitzer, H. R., and Hengstenberg, W. (1993) The solution structure of the histidine-containing protein (HPr) from *Staphylococcus aureus* as determined by two-dimensional ¹H-NMR spectroscopy. *Eur. J. Biochem.* **216**, 205-214
13. Wittekind, M., Rajagopal, P., Branchini, B. R., Reizer, J., Saier, M. H., Jr., and Klevit, R. E. (1992) Solution structure of the phosphocarrier protein HPr from *Bacillus subtilis* by two-dimensional NMR spectroscopy. *Protein Sci.* **1**, 1363-1376
14. Eberstadt, M., Grdadolnik, S. G., Gemmecker, G., Kessler, H., Buhr, A., and Erni, B. (1996) Solution structure of the IIB domain of the glucose transporter of *Escherichia coli*. *Biochemistry* **35**, 11286-11292
15. Hu, J., Hu, K., Williams, D. C., Jr., Komlos, M. E., Cai, M., and Clore, G. M. (2008) Solution NMR structures of productive and non-productive complexes between the A and B domains of the cytoplasmic subunit of the mannose transporter of the *Escherichia coli* phosphotransferase system. *J. Biol. Chem.* **283**, 11024-11037
16. Cai, M., Williams, D. C., Jr., Wang, G., Lee, B. R., Peterkofsky, A., and Clore, G. M. (2003) Solution structure of the phosphoryl transfer complex between the signal-transducing protein IIA^{Glucose} and the cytoplasmic domain of the glucose transporter IICB^{Glucose} of the *Escherichia coli* glucose phosphotransferase system. *J. Biol. Chem.* **278**, 25191-25206
17. Garrett, D. S., Seok, Y. J., Liao, D. I., Peterkofsky, A., Gronenborn, A. M., and Clore, G. M. (1997) Solution structure of the 30 kDa N-terminal domain of enzyme I of the *Escherichia coli* phosphoenolpyruvate:sugar phosphotransferase system by multidimensional NMR. *Biochemistry* **36**, 2517-2530
18. Schwieters, C. D., Suh, J. Y., Grishaev, A., Ghirlando, R., Takayama, Y., and Clore, G. M. (2010) Solution structure of the 128 kDa enzyme I dimer from *Escherichia coli* and its 146 kDa complex with HPr using residual dipolar couplings and small- and wide-angle X-ray scattering. *J Am Chem Soc* **132**, 13026-13045
19. Takayama, Y., Schwieters, C. D., Grishaev, A., Ghirlando, R., and Clore, G. M. (2010) Combined use of residual dipolar couplings and solution X-ray scattering to rapidly probe rigid-body conformational transitions in a non-phosphorylatable active-site mutant of the 128 kDa Enzyme I dimer. *J Am Chem Soc*
20. Tang, C., Williams, D. C., Jr., Ghirlando, R., and Clore, G. M. (2005) Solution structure of enzyme IIA^{Chitobiose} from the N,N'-diacetylchitobiose branch of the *Escherichia coli* phosphotransferase system. *J Biol Chem* **280**, 11770-11780
21. van Montfort, R. L., Pijning, T., Kalk, K. H., Hangyi, I., Kouwijzer, M. L., Robillard, G. T., and Dijkstra, B. W. (1998) The structure of the *Escherichia coli* phosphotransferase IIA^{mannitol} reveals a novel fold with two conformations of the active site. *Structure* **6**, 377-388
22. Teplyakov, A., Lim, K., Zhu, P. P., Kapadia, G., Chen, C. C., Schwartz, J., Howard, A., Reddy, P. T., Peterkofsky, A., and Herzberg, O. (2006) Structure of phosphorylated enzyme I, the phosphoenolpyruvate:sugar phosphotransferase system sugar translocation signal protein. *Proc. Natl. Acad. Sci. U. S. A.* **103**, 16218-16223
23. Oberholzer, A. E., Bumann, M., Schneider, P., Bachler, C., Siebold, C., Baumann, U., and Erni, B. (2005) Crystal structure of the phosphoenolpyruvate-binding enzyme I-domain from the *Thermoanaerobacter tengcongensis* PEP: sugar phosphotransferase system (PTS). *J. Mol. Biol.* **346**, 521-532
24. Oberholzer, A. E., Schneider, P., Siebold, C., Baumann, U., and Erni, B. (2009) Crystal structure of enzyme I of the phosphoenolpyruvate:sugar phosphotransferase system in the dephosphorylated state. *J. Biol. Chem.*
25. Orriss, G. L., Erni, B., and Schirmer, T. (2003) Crystal structure of the IIB^{Sor} domain of the sorbose permease from *Klebsiella pneumoniae* solved to 1.75Å resolution. *J. Mol. Biol.* **327**, 1111-1119
26. Liao, D. I., Kapadia, G., Reddy, P., Saier, M. H., Jr., Reizer, J., and Herzberg, O. (1991) Structure of the IIA domain of the glucose permease of *Bacillus subtilis* at 2.2-Å resolution. *Biochemistry* **30**, 9583-9594
27. Liao, D. I., Silverton, E., Seok, Y. J., Lee, B. R., Peterkofsky, A., and Davies, D. R. (1996) The first step in sugar transport: crystal structure of the amino terminal domain of enzyme I of the *E. coli* PEP: sugar phosphotransferase system and a model of the phosphotransfer complex with HPr. *Structure* **4**, 861-872

28. Marquez, J., Reinelt, S., Koch, B., Engelmann, R., Hengstenberg, W., and Scheffzek, K. (2006) Structure of the full-length enzyme I of the phosphoenolpyruvate-dependent sugar phosphotransferase system. *J. Biol. Chem.* **281**, 32508-32515
29. Herzberg, O., Reddy, P., Sutrina, S., Saier, M. H., Jr., Reizer, J., and Kapadia, G. (1992) Structure of the histidine-containing phosphocarrier protein HPr from *Bacillus subtilis* at 2.0-Å resolution. *Proc. Natl. Acad. Sci. U. S. A.* **89**, 2499-2503
30. Jia, Z., Quail, J. W., Waygood, E. B., and Delbaere, L. T. (1993) The 2.0-Å resolution structure of *Escherichia coli* histidine-containing phosphocarrier protein HPr. A redetermination. *J. Biol. Chem.* **268**, 22490-22501
31. Worthylake, D., Meadow, N. D., Roseman, S., Liao, D. I., Herzberg, O., and Remington, S. J. (1991) Three-dimensional structure of the *Escherichia coli* phosphocarrier protein III^{glc}. *Proc. Natl. Acad. Sci. U. S. A.* **88**, 10382-10386
32. Sliz, P., Engelmann, R., Hengstenberg, W., and Pai, E. F. (1997) The structure of enzyme IIA^{lactose} from *Lactococcus lactis* reveals a new fold and points to possible interactions of a multicomponent system. *Structure* **5**, 775-788
33. Nunn, R. S., Markovic-Housley, Z., Genovesio-Taverne, J. C., Flukiger, K., Rizkallah, P. J., Jansonius, J. N., Schirmer, T., and Erni, B. (1996) Structure of the IIA domain of the mannose transporter from *Escherichia coli* at 1.7 angstroms resolution. *J. Mol. Biol.* **259**, 502-511
34. Schauder, S., Nunn, R. S., Lanz, R., Erni, B., and Schirmer, T. (1998) Crystal structure of the IIB subunit of a fructose permease (IIB^{Lev}) from *Bacillus subtilis*. *J. Mol. Biol.* **276**, 591-602
35. Navdaeva, V., Zurbriggen, A., Waltersperger, S., Schneider, P., Oberholzer, A. E., Bahler, P., Bachler, C., Grieder, A., Baumann, U., and Erni, B. (2011) Phosphoenolpyruvate:sugar phosphotransferase system from the hyperthermophilic *Thermoanaerobacter tengcongensis*. *Biochemistry* **50**, 1184-1193
36. Garrett, D. S., Seok, Y. J., Peterkofsky, A., Gronenborn, A. M., and Clore, G. M. (1999) Solution structure of the 40,000 M_r phosphoryl transfer complex between the N-terminal domain of enzyme I and HPr. *Nature Struct. Biol.* **6**, 166-173
37. Wang, G., Louis, J. M., Sondej, M., Seok, Y. J., Peterkofsky, A., and Clore, G. M. (2000) Solution structure of the phosphoryl transfer complex between the signal transducing proteins HPr and IIA^{glucose} of the *Escherichia coli* phosphoenolpyruvate:sugar phosphotransferase system. *EMBO J.* **19**, 5635-5649
38. Cornilescu, G., Lee, B. R., Cornilescu, C. C., Wang, G., Peterkofsky, A., and Clore, G. M. (2002) Solution structure of the phosphoryl transfer complex between the cytoplasmic A domain of the mannitol transporter II^{Mannitol} and HPr of the *Escherichia coli* phosphotransferase system. *J. Biol. Chem.* **277**, 42289-42298
39. Williams, D. C., Jr., Cai, M., Suh, J. Y., Peterkofsky, A., and Clore, G. M. (2005) Solution NMR structure of the 48-kDa IIA^{Mannose}-HPr complex of the *Escherichia coli* mannose phosphotransferase system. *J. Biol. Chem.* **280**, 20775-20784
40. Suh, J. Y., Cai, M., Williams, D. C., Jr., and Clore, G. M. (2006) Solution structure of a post-transition state analog of the phosphoryl transfer reaction between the A and B cytoplasmic domains of the mannitol transporter II^{Mannitol} of the *Escherichia coli* phosphotransferase system. *J Biol Chem* **281**, 8939-8949
41. Suh, J. Y., Iwahara, J., and Clore, G. M. (2007) Intramolecular domain-domain association/dissociation and phosphoryl transfer in the mannitol transporter of *Escherichia coli* are not coupled. *Proc Natl Acad Sci U S A* **104**, 3153-3158
42. Suh, J. Y., Cai, M., and Clore, G. M. (2008) Impact of phosphorylation on structure and thermodynamics of the interaction between the N-terminal domain of enzyme I and the histidine phosphocarrier protein of the bacterial phosphotransferase system. *J Biol Chem* **283**, 18980-18989
43. Jung, Y. S., Cai, M., and Clore, G. M. (2010) Solution structure of the IIA^{Chitobiose}-IIB^{Chitobiose} complex of the N,N'-diacetylchitobiose branch of the *Escherichia coli* phosphotransferase system. *J Biol Chem* **285**, 4173-4184
44. Tang, C., Iwahara, J., and Clore, G. M. (2006) Visualization of transient encounter complexes in protein-protein association. *Nature* **444**, 383-386
45. Suh, J. Y., Tang, C., and Clore, G. M. (2007) Role of electrostatic interactions in transient encounter complexes in protein-protein association investigated by paramagnetic relaxation enhancement. *J Am Chem Soc* **129**, 12954-12955
46. Fawzi, N. L., Doucleff, M., Suh, J. Y., and Clore, G. M. (2010) Mechanistic details of a protein-protein association pathway revealed by paramagnetic relaxation enhancement titration measurements. *Proc Natl Acad Sci U S A* **107**, 1379-1384
47. Garrett, D. S., Seok, Y. J., Peterkofsky, A., Clore, G. M., and Gronenborn, A. M. (1997) Identification by NMR of the binding surface for the histidine-containing phosphocarrier protein HPr on the N-terminal domain of enzyme I of the *Escherichia coli* phosphotransferase system. *Biochemistry* **36**, 4393-4398

48. Goto, N. K., Gardner, K. H., Mueller, G. A., Willis, R. C., and Kay, L. E. (1999) A robust and cost-effective method for the production of Val, Leu, Ile(δ 1) methyl-protonated ^{15}N -, ^{13}C -, ^2H -labeled proteins. *J. Biomol. NMR* **13**, 369-374
49. Delaglio, F., Grzesiek, S., Vuister, G. W., Zhu, G., Pfeifer, J., and Bax, A. (1995) NMRPipe: a multidimensional spectral processing system based on UNIX pipes. *J. Biomol. NMR* **6**, 277-293
50. Garrett, D. S., Powers, R., Gronenborn, A. M., and Clore, G. M. (1991) A common sense approach to peak picking in two-, three- and four-dimensional spectra using automatic computer analysis of contour diagrams. *J. Magn. Reson.* **95**, 214-220
51. Clore, G. M., and Gronenborn, A. M. (1991) Structures of larger proteins in solution: three- and four-dimensional heteronuclear NMR spectroscopy. *Science* **252**, 1390-1399
52. Yang, D., and Kay, L. E. (1999) Improved ^1H -detected triple resonance TROSY-based experiments. *J. Biomol. NMR* **13**, 3-10
53. Clore, G. M., and Gronenborn, A. M. (1998) Determining the structures of large proteins and protein complexes by NMR. *Trends Biotechnol.* **16**, 22-34
54. Cai, M., Huang, Y., Zheng, R., Wei, S. Q., Ghirlando, R., Lee, M. S., Craigie, R., Gronenborn, A. M., and Clore, G. M. (1998) Solution structure of the cellular factor BAF responsible for protecting retroviral DNA from autointegration. *Nature Struct. Biol.* **5**, 903-909
55. Clore, G. M., and Gronenborn, A. M. (1998) New methods of structure refinement for macromolecular structure determination by NMR. *Proc. Natl. Acad. Sci. U. S. A.* **95**, 5891-5898
56. Clore, G. M., Gronenborn, A. M., Nilges, M., and Ryan, C. A. (1987) Three-dimensional structure of potato carboxypeptidase inhibitor in solution. A study using nuclear magnetic resonance, distance geometry, and restrained molecular dynamics. *Biochemistry* **26**, 8012-8023
57. Nilges, M. (1993) A calculation strategy for the structure determination of symmetric dimers by ^1H NMR. *Proteins* **17**, 297-309
58. Shen, Y., Delaglio, F., Cornilescu, G., and Bax, A. (2009) TALOS+: a hybrid method for predicting protein backbone torsion angles from NMR chemical shifts. *J. Biomol. NMR* **44**, 213-223
59. Clore, G. M. (2000) Accurate and rapid docking of protein-protein complexes on the basis of intermolecular nuclear overhauser enhancement data and dipolar couplings by rigid body minimization. *Proc. Natl. Acad. Sci. U. S. A.* **97**, 9021-9025
60. Schwieters, C. D., and Clore, G. M. (2001) Internal coordinates for molecular dynamics and minimization in structure determination and refinement. *J. Magn. Reson.* **152**, 288-302
61. Schwieters, C. D., Kuszewski, J., and Clore, G. M. (2006) Using Xplor-NIH for NMR molecular structure determination. *Progr. NMR. Spectros.* **48**, 47-62
62. Clore, G. M., and Kuszewski, J. (2002) χ_1 rotamer populations and angles of mobile surface side chains are accurately predicted by a torsion angle database potential of mean force. *J. Am. Chem. Soc.* **124**, 2866-2867
63. Schwieters, C. D., and Clore, G. M. (2008) A pseudopotential for improving the packing of ellipsoidal protein structures determined from NMR data. *J. Phys. Chem. B* **112**, 6070-6073
64. Schwieters, C. D., and Clore, G. M. (2001) The VMD-XPLOR visualization package for NMR structure refinement. *J. Magn. Reson.* **149**, 239-244
65. Nicholls, A., Sharp, K. A., and Honig, B. (1991) Protein folding and association: insights from the interfacial and thermodynamic properties of hydrocarbons. *Proteins* **11**, 281-296
66. Schwieters, C. D., and Clore, G. M. (2002) Reweighted atomic densities to represent ensembles of NMR structures. *J. Biomol. NMR* **23**, 221-225
67. Begley, G. S., Hansen, D. E., Jacobson, G. R., and Knowles, J. R. (1982) Stereochemical course of the reactions catalyzed by the bacterial phosphoenolpyruvate:glucose phosphotransferase system. *Biochemistry* **21**, 5552-5556
68. Herzberg, O. (1992) An atomic model for protein-protein phosphoryl group transfer. *J. Biol. Chem.* **267**, 24819-24823
69. Grzesiek, S., Stahl, S. J., Wingfield, P. T., and Bax, A. (1996) The CD4 determinant for downregulation by HIV-1 Nef directly binds to Nef. Mapping of the Nef binding surface by NMR. *Biochemistry* **35**, 10256-10261
70. Clore, G. M., and Garrett, D. S. (1999) R-factor, free R and complete cross-validation for dipolar coupling refinement of NMR structures. *J. Am. Chem. Soc.* **121**, 9008-9012
71. Laskowski, R. A., McArthur, M. W., Moss, D. S., and Thornton, J. M. (1993) PROCHECK: a program to check the stereochemical quality of protein structures. *J. Appl. Crystallogr.* **26**, 283-291

FOOTNOTES

*This work was supported by the intramural program of NIDDK, NIH and the Intramural AIDS Targeted Antiviral Program of the Office of the Director of the National Institutes of Health (to G.M.C.).

The atomic coordinates and NMR experimental restraints (accession code 2lrk for the unphosphorylated complex and 2lrl for the phosphoryl transition state complex) have been deposited in the Protein Data Bank, Research Collaboratory for Structural Bioinformatics, Rutgers University, New Brunswick, NJ (<http://www.rcsb.org/>)

†These authors contributed equally to the work in this paper.

‡ Present address: Korean Basic Science Institute, Seoul Center, 126-16, Anamdong 5-ga, Seongbuk-gu, Seoul, South Korea.

¶To whom correspondence should be addressed: Laboratory of Chemical Physics, Building 5, Rm B1-30I, NIDDK, National Institutes of Health, Bethesda, MD 20892-0520. Tel: 301-496-0782; Fax: 301-496-0825; E-mail: mariusc@mail.nih.gov.

¹The abbreviations used are: PTS, phosphoenolpyruvate:sugar phosphotransferase system; enzyme I, EI; HPr, histidine-containing phosphocarrier protein; Chb, N,N'-diacetylchitobiose; IIA^{Chb}, IIB^{Chb} and IIC^{Chb}, A, B and C domains, respectively, of the N,N'-diacetylchitobiose transporter II^{Chb}; IIA^{Chb*}, double mutant of IIA^{Chb} comprising a 13-residue deletion at the N-terminus and an Asp to Leu mutation at position 92 (wild type numbering). NOE, nuclear Overhauser effect; HSQC, heteronuclear single quantum coherence; TROSY, transverse relaxation optimized spectroscopy; rms, root mean square; AA, amino acid; RDC, residual dipolar coupling.

Figure legends

Fig. 1. Binding of IIA^{Chb*}(H89E) to ¹⁵N-labeled HPr. Backbone amide chemical shift perturbations upon titrating unlabeled IIA^{Chb*}(H89E) into a solution of ¹⁵N-labeled HPr at 20°C. The chemical shifts were monitored using ¹H-¹⁵N HSQC spectroscopy at a spectrometer ¹H frequency of 600 MHz. $\Delta\delta_{H/N} = [(\Delta\delta^{15N})^2/25 + (\Delta\delta^1H)^2/2]^{1/2}$ in parts per billion (ppb) (69). The IIA^{Chb*}(H89E):HPr molar ratios, expressed in terms of subunit concentration of IIA^{Chb*}(H89E), are 0, 0.5, 1.0, 1.5, 2.0, 2.5 and 3.0, with corresponding concentrations of 0.0, 0.24, 0.47, 0.68, 0.87, 1.05 and 1.23 mM in subunits for IIA^{Chb*}(H89E), and 0.50, 0.48, 0.47, 0.45, 0.44, 0.42 and 0.41 mM for HPr. The solid lines represent the results of a global non-linear least squares best-fit to all the titration data simultaneously, using a simple equilibrium binding model. The optimized K_D value is 0.7 ± 0.1 mM.

Fig. 2. Intermolecular NOEs in the IIA^{Chb*}(H89E)-HPr complex. NOEs in a 3D ¹²C-filtered/¹³C-separated NOE experiment recorded in D₂O are specifically observed from protons attached to ¹²C (in the F₁ dimension) to methyl protons attached to ¹³C (in the F₃ dimension). Strips are shown for NOEs involving the ¹³Cδ1 methyl group of Ile72 (at 12.48 ppm) and one of the ¹³Cγ methyl groups of Val21 (at 23.63 ppm) of IIA^{Chb*}(H89E). The amino-acid (AA) specific labeling schemes used for [¹H-AA]/[²H, ¹²C, ¹⁴N]-HPr are shown above each strip.

Fig. 3. Solution structure of the IIA^{Chb*}(H89E)-HPr complex. *A*, Stereoview of a superposition of the backbone (N, Cα, C) atoms of the final 100 simulated annealing structures with the A, B and C subunits of the IIA^{Chb*}(H89E) symmetric trimer in *blue*, *gold* and *green*, respectively, and HPr in *red*. HPr is shown interacting with the A and C subunits of IIB^{Chb*}. The *purple* meshes represent the atomic density probability maps (66) for the two active site residues, H89E of subunit A of IIA^{Chb*}(H89E) and *His15* of HPr. (The probability maps are drawn at a value of 20% maximum). Note that since IIA^{Chb*}(H89E) is a symmetric trimer there are three identical binding sites formed at the interfaces between the A and C subunits, the C and B subunits, and the B and A subunits. *B*, Ribbon diagrams of the complex showing two HPr molecules bound to the IIA^{Chb*}(H89E) trimer (left panel) and an orthogonal view depicting three molecules of HPr bound to the IIA^{Chb*}(H89E) trimer (right panel). The color coding is the same as in (*A*). *D*, Stereoview showing a reweighted atomic probability density map (drawn at a value of 20% maximum and calculated from the final 100 simulated annealing structures) for some of the interfacial side chains displayed as *blue* and *green* meshes for the A and B subunits for IIA^{Chb*}(H89E) and as a *red* mesh for HPr. The backbones are shown as tubes color coded as in (*A*); the side chains of the restrained regularized mean structure are color coded according to atom type (carbon, *grey*; oxygen, *red*; nitrogen, *blue*; sulfur, *yellow*). Residues of HPr are labeled in *italics*.

Fig. 4. Interaction surfaces for the IIA^{Chb*}(H89E)-HPr complex. *A*, Interaction surface (formed by the A and C subunits) on IIA^{Chb*}(H89E) for HPr. *B*, interaction surface on HPr for IIA^{Chb*}(H89E). The surfaces are color coded as follows: hydrophobic residues, *green*; uncharged residues bearing a polar functional group, *cyan*; negatively charged residues, *red*; positively charged residues, *blue*. Relevant portions of the backbone and the active site residue of the interacting partner are displayed as tubes and bonds, respectively. Residues of HPr are labeled in *italics*. Residues from the C subunit of IIB^{Chb*}(H89E) are indicated by an apostrophe after the residue number; in addition, the surfaces of the A and C subunits of IIA^{Chb*} that do not constitute the interaction surface are colored in *dark grey* and *light grey*, respectively.

Fig. 5. The IIA^{Chb*}(H89E)-HPr interface. *A*, Stereoview of the interface between the A subunit of IIA^{Chb*}(H89E) and HPr with the respective backbones shown as *blue* and *red* ribbons, respectively. *B*, Stereoview of the interface between the C subunit of IIA^{Chb*}(H89E) and HPr with the respective backbones shown as *green* and *red* ribbons, respectively. The dashed lines indicate potential intermolecular hydrogen bonds or salt bridges. The side chain atoms are colored according to atom type (carbon, *grey*; oxygen, *red*; nitrogen, *blue*; sulfur, *yellow*). Residues of HPr are labeled in *italics*. *C*, Diagrammatic representation of the intermolecular contacts between the A and C subunits of IIA^{Chb*}(H89E) and HPr. Residues involved in side chain-side chain electrostatic interactions are colored in *blue* (donor) or *red* (acceptor). The active site residues, H89E of IIA^{Chb*}(H89E), and *His15* of HPr are shown in bold letters.

Fig. 6. The phosphoryl transition state of the IIA^{Chb*}-HPr complex. *A*, Environment surrounding the His89^A-P-His15 pentacoordinate phosphoryl transition state. The backbone is displayed as transparent tubes with HPr in *red*, and the A and C subunits of IIA^{Chb*} in *blue* and *green*, respectively. *B*, Identical view to (*A*) showing a superposition of the structure of the IIA^{Chb*}(H89E)-HPr complex (transparent tubes and bonds) with the structure of the IIA^{Chb*}-P-HPr transition state (opaque tubes and bonds). Exactly the same experimental restraints are used to calculate the two structures, but, in addition, the calculations for the transition state include geometric restraints specifying the geometry of the phosphoryl transition state and backbone torsion angle degrees of freedom for residues 13-17 of HPr encompassing the active side His15. Color coding: *red*, HPr; *blue*, A subunit of IIA^{Chb*}; *green*, C subunit of IIA^{Chb*}. Side chains are displayed as stick diagrams with the atoms color coded according to type (carbon, *grey*; nitrogen, *blue*; oxygen, *red*; phosphorus, *gold*; sulfur, *yellow*). Residues of HPr are labeled in *italics*. Dashed *black* lines indicate hydrogen bonds to the phosphoryl group in the transition state, and the dashed *grey* line indicates a potential intermolecular hydrogen bond between the carboxamide group of Asn12 of HPr and the Met98(Sδ) atom of the C subunit of IIA^{Chb*}.

Fig. 7 Comparison of the IIA^{Chb*}-HPr and IIA^{Chb*}-IIB^{Chb} complexes. *A*, Overall stereoview with IIA^{Chb*} from the two complexes best-fitted to one another, and, *B*, close up of the His-P-His and His-P-Cys phosphoryl transition states for the IIA^{Chb*}-HPr and IIA^{Chb*}-IIB^{Chb} complexes, respectively. The backbone is displayed as a ribbon diagram and the His-P-His and His-P-Cys transition states as stick diagrams with the atoms color coded according to type (carbon, *grey*; nitrogen, *blue*; oxygen, *red*; phosphorus, *gold*; sulfur, *yellow*). For the IIA^{Chb*}-HPr complex, IIA^{Chb*} and HPr are shown in *red* and *blue*, respectively; for the IIA^{Chb*}-IIB^{Chb} complex, IIA^{Chb*} and IIB^{Chb} are shown in *grey* and *purple*, respectively. The coordinates of the IIA^{Chb*}-IIB^{Chb} complex are taken from ref. (43) (PDB code 2WWV). The small differences in the IIA^{Chb*} coordinates from the two structures is within coordinate error. Also note that the region which displays the largest apparent differences is the loop from residues 77-84 of IIA^{Chb*} which is disordered in solution.

Table 1

Labeling schemes for samples used for intermolecular NOE measurements on the IIA^{Chb} (H89E)-HPr complex*

Sample	Isotope labeling	
	IIA ^{Chb*} (H89E)	HPr
1	[¹³ CH ₃ -ILV]/[² H/ ¹³ C/ ¹⁵ N]	[¹ H-Ile, Gly, Phe]/[² H/ ¹² C/ ¹⁴ N]
2	[¹³ CH ₃ -ILV]/[² H/ ¹³ C/ ¹⁵ N]	[¹ H-Leu, Met, Tyr]/[² H/ ¹² C/ ¹⁴ N]
3	[¹³ CH ₃ -ILV]/[² H/ ¹³ C/ ¹⁵ N]	[¹ H-Val, Ala, His]/[² H/ ¹² C/ ¹⁴ N]
4	[¹ H-Ile, Gly, Phe]/[² H/ ¹² C/ ¹⁴ N]	[¹³ CH ₃ -ILV]/[² H/ ¹³ C/ ¹⁵ N]
5	[¹ H-Leu, Met, Tyr]/[² H/ ¹² C/ ¹⁴ N]	[¹³ CH ₃ -ILV]/[² H/ ¹³ C/ ¹⁵ N]
6	[¹ H-Val, Ala, His]/[² H/ ¹² C/ ¹⁴ N]	[¹³ CH ₃ -ILV]/[² H/ ¹³ C/ ¹⁵ N]
7	[¹ H-Ile, Gly, Phe]/[² H/ ¹² C/ ¹⁴ N]	U-[¹ H/ ¹³ C/ ¹⁵ N]
8	[¹ H-Leu, Met, Tyr]/[² H/ ¹² C/ ¹⁴ N]	U-[¹ H/ ¹³ C/ ¹⁵ N]
9	U-[² H/ ¹³ C/ ¹⁵ N]	U-[¹ H/ ¹² C/ ¹⁴ N]

Table 2*Structural statistics*

The notation of the NMR structures is as follows: <SA> are the final 100 simulated annealing structures for the IIA^{Chb*}(H89E)-HPr complex and <SA_{phos}> are the final 70 simulated annealing structures for the corresponding phosphoryl transition state.

	<SA>	<SA _{phos} >
Number of experimental NMR restraints		
Intermolecular interproton distance restraints	42	
IIA ^{Chb*} intramolecular interproton distance restraints ^a	276 x 3	
IIA ^{Chb*} torsion angle restraints ^a	245 x 3	
HPr torsion angle restraints ^b	36	
¹ D _{NH} RDCs for IIA ^{Chb*} ^a	84 x 3	
¹ D _{NC} RDCs for IIA ^{Chb*} ^a	85 x 3	
¹ D _{CαC} RDCs for IIA ^{Chb*} ^a	83 x 3	
¹³ Cα/ ¹³ Cβ chemical shift restraints for IIA ^{Chb*} ^a	195 x 3	
Experimental restraints		
R.m.s. deviation from interproton distance restraints (Å) ^c	0.010±0.002	0.011±0.001
R.m.s. deviation from torsion angle restraints (°) ^c	0.25±0.04	0.25±0.04
R.m.s. deviation from ¹³ Cα/ ¹³ Cβ shift restraints (ppm)	1.12±0.02 / 0.66±0.02	1.12±0.02 / 0.63±0.01
¹ D _{NH} RDC R-factor (%) ^d	7.4±0.1	7.4±0.08
¹ D _{NC} RDC R-factor (%) ^d	17.1±1.3	16.8±0.97
¹ D _{CαC} RDC R-factor (%) ^d	16.2±0.9	15.9±0.52
Deviations from idealized covalent geometry^e		
bonds (Å)	0.006±0	0.006±0
angles (deg.)	0.63±0	0.63±0
impropers (deg.)	0.63±0	0.62±0
Measures of structural quality^f		
Intermolecular repulsion energy (kcal·mol ⁻¹)	1.3±0.4	1.4±0.4
Intermolecular Lennard-Jones energy (kcal·mol ⁻¹)	-16.2±5.2	-16.7±4.5
Number of bad contacts per 100 residues	3.6±1.1	3.1±1.1
% residues in most favorable region of Ramachandran map	94.5±1.0	94.3±1.3
Coordinate precision of the complex (Å)^g		
Backbone (N, Cα, C', O) atoms	0.56	0.49
Interfacial sidechain heavy atoms of IIA ^{Chb*} and HPr ^g	1.25	1.07
Side chain heavy atoms of IIA ^{Chb*}	1.32	1.24

^aThe intramolecular experimental restraints (NOE-derived interproton distances, torsion angles, ¹³Cα/¹³Cβ chemical shifts and residual dipolar couplings) for IIA^{Chb*} in the complex are taken from the structure determination of free IIA^{Chb*}. The interproton distance restraints comprise 82 x 3 sequential ($|i-j|=1$), 86 x 3 medium range ($1 < |i-j| \leq 5$), and 30 x 3 long range ($|i-j| > 5$) intrasubunit restraints, 78 x 3 intersubunit distances and 154 x 3 distance restraints for 77 x 3 backbone hydrogen bonds within the three helices. The torsion angle restraints comprise 87 x 3 ϕ , 82 x 3 ψ , 76 x 3 χ angles.

^bThe torsion angle restraints for HPr comprise 26 interfacial side chain torsion angles, supplemented, in the case of the calculations of the phosphoryl transition state, by 5 ϕ and 5 ψ backbone torsion angles (derived

Footnotes to Table 2 (cont.)

from chemical shifts in the complex using TALOS+ (58)) for residues 13-17 encompassing the active site His15. The side chains of HPr given torsional degrees of freedom comprise residues 11-17, 20-21, 23-24, 27, 45-48, 51-57 and 85.

^cNone of the structures exhibit interproton distance violations >0.3 Å or torsion angle violations $>5^\circ$.

^dThe RDC R-factor (70) is defined as the ratio of the rmsd between observed and calculated values and the expected rmsd for a random distribution of vectors. The latter is given by $[2D_a^2(4+3\eta^2)/5]^{1/2}$, where D_a and η are the magnitude of the alignment tensor and the rhombicity, respectively. The values of D_a and η for the free IIA^{Chb*} trimer are -12.1 Hz and 0, respectively (note the rhombicity for a symmetric trimer is always 0). The R-factor scales between 0 and 100%.

^eThe His-P-His phosphoryl transition state formed between the Ne2 atom of His89 of subunit A of IIA^{Chb*} and the Nδ1 atom of His15 of HPr is calculated using the same experimental restraints as those used for the unphosphorylated complex with the addition of covalent geometry restraints to describe the pentacoordinate phosphoryl group in a trigonal bipyramidal geometry (37): $r_{\text{Ne2(His89)-P}}, r_{\text{Nδ1(His15)-P}} \leq 3.5$ Å, $r_{\text{P-O}} = 1.48$ Å; $\text{Nδ1(His15)-P-Ne2(His89)} = 180^\circ$, $\text{Nδ1(His15)-P-O} = 90^\circ$, $\text{Ne2(His89)-P-O} = 90^\circ$, $\text{Cγ(His15)-Nδ1(His15)-P} = 127.35^\circ$, $\text{Cε1(His15)-Nδ1(His15)-P} = 127.35^\circ$, $\text{Cδ2(His89)-Ne2(His89)-P} = 126.35^\circ$, $\text{Cε1(His89)-Ne2(His89)-P} = 126.35^\circ$. In addition improper torsion angle restraints are used to ensure that the phosphorus atom lies in the same plane as the imidazole ring of both His89^A and His15.

^fThe intermolecular repulsion energy is given by the value of the quartic van der Waals repulsion term calculated with a force constant of $4 \text{ kcal} \cdot \text{mol}^{-1} \cdot \text{Å}^{-4}$ and a van der Waals radius scale factor of 0.78 (61). The intermolecular Lennard-Jones van der Waals interaction energy is calculated using the CHARMM19/20 parameters and is *not* included in the target function used to calculate the structures. The number of bad contacts per 100 residues and the percentage of residues in the most favorable region of the Ramachandran plot are calculated using PROCHECK (71). The ϕ/ψ , χ_1/χ_2 , χ_1 and χ_3/χ_4 PROCHECK *g*-factors are 0.76 ± 0.04 , 0.60 ± 0.06 , 0.21 ± 0.10 and 0.42 ± 0.07 , respectively.

^gDefined as the average r.m.s. difference between the final ensemble of simulated annealing structures and the mean coordinates positions.

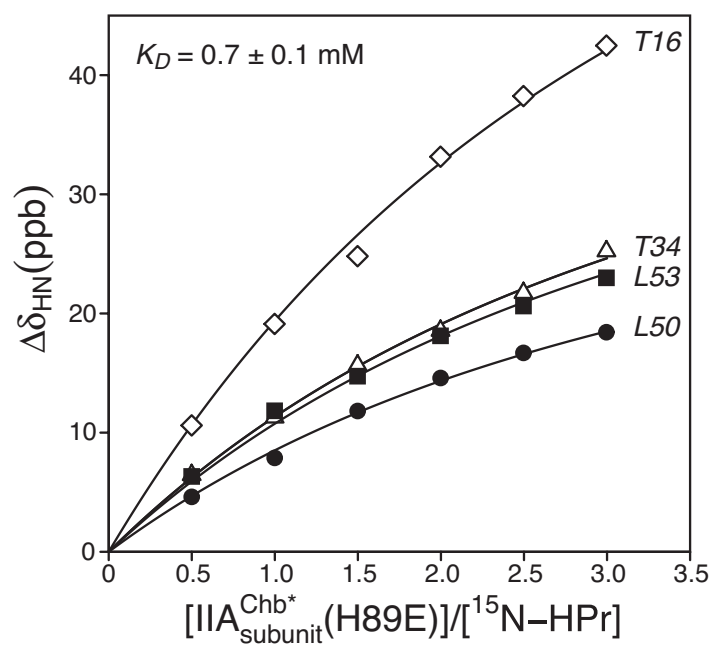


Fig. 1

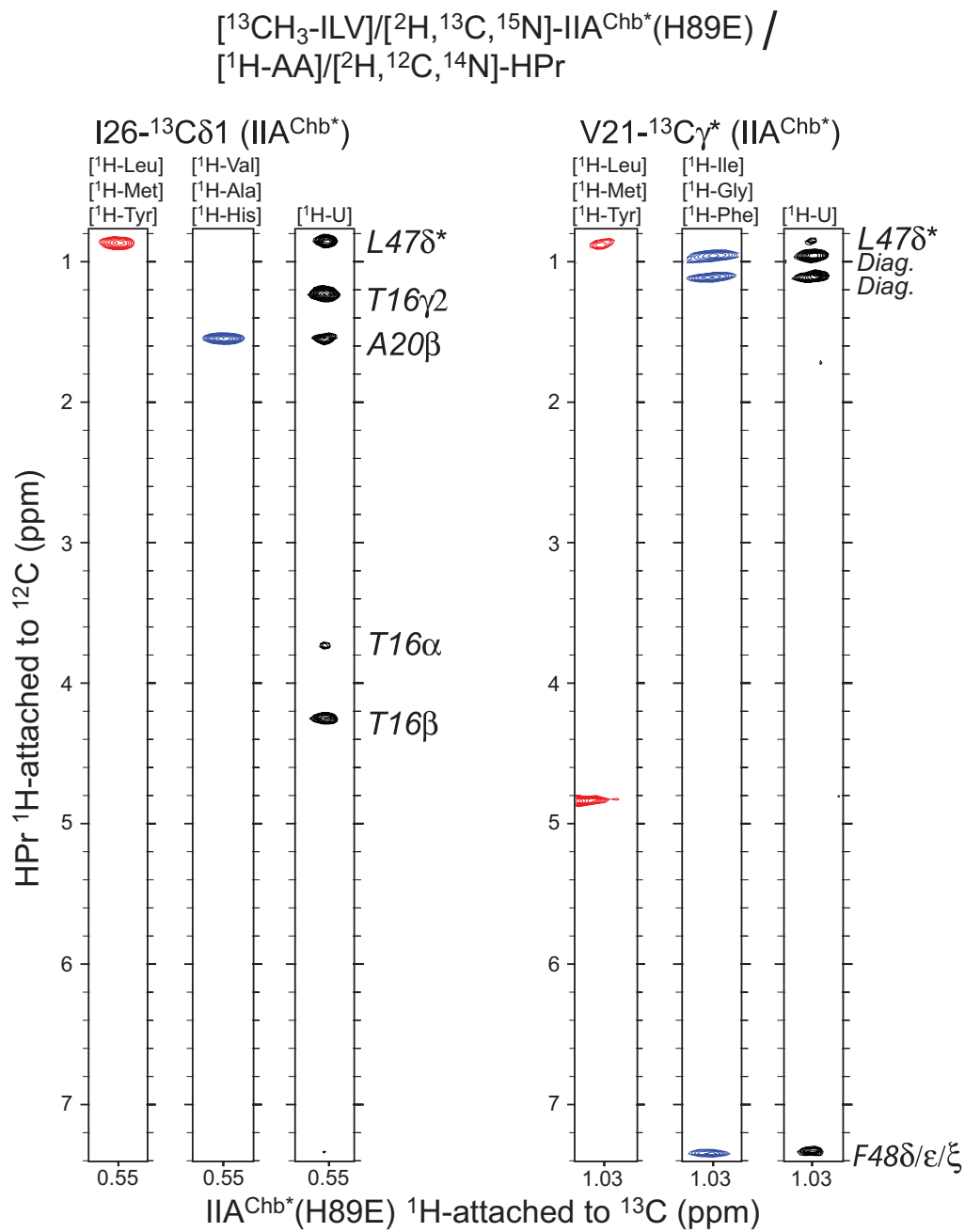


Fig. 2

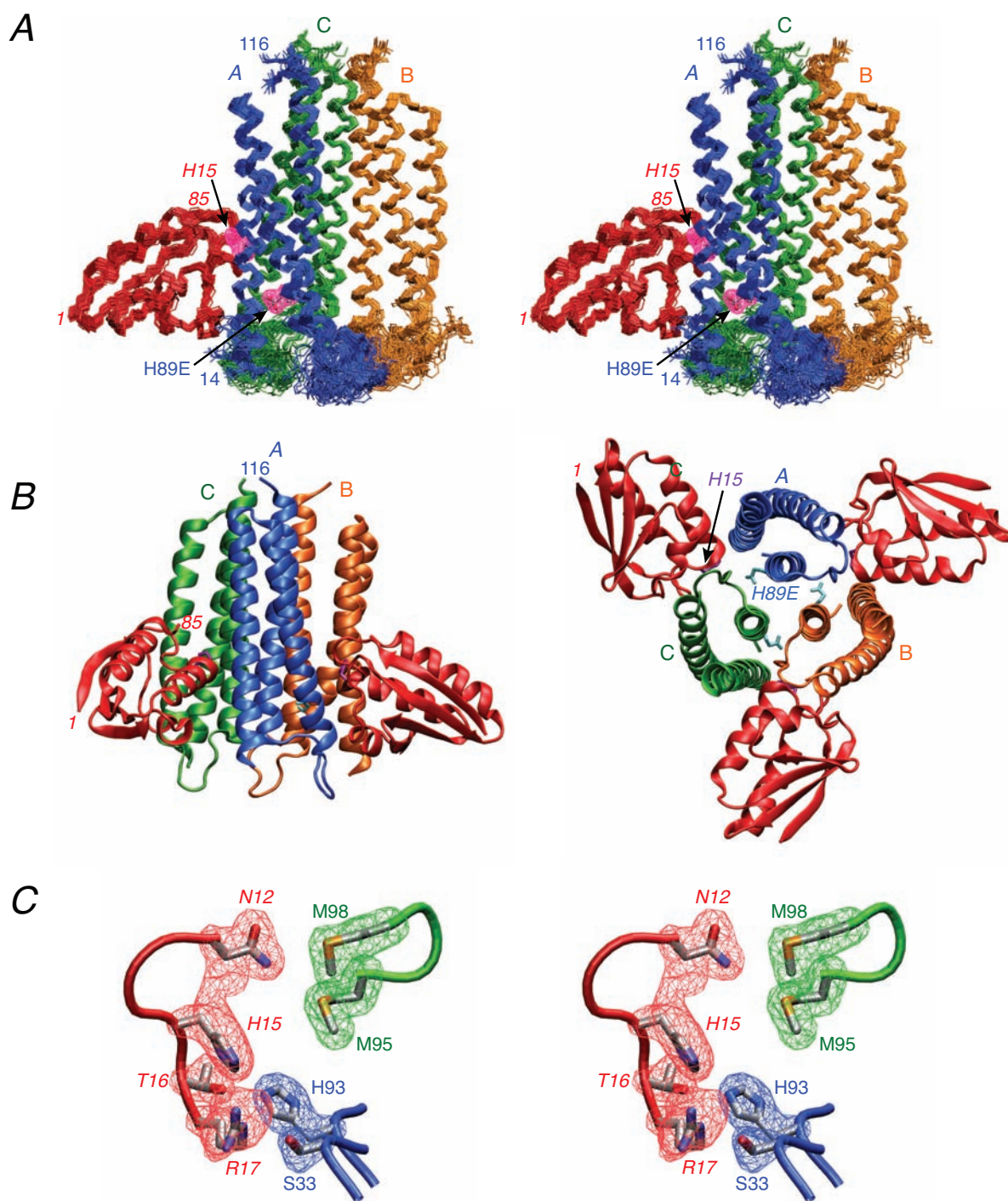


Fig. 3

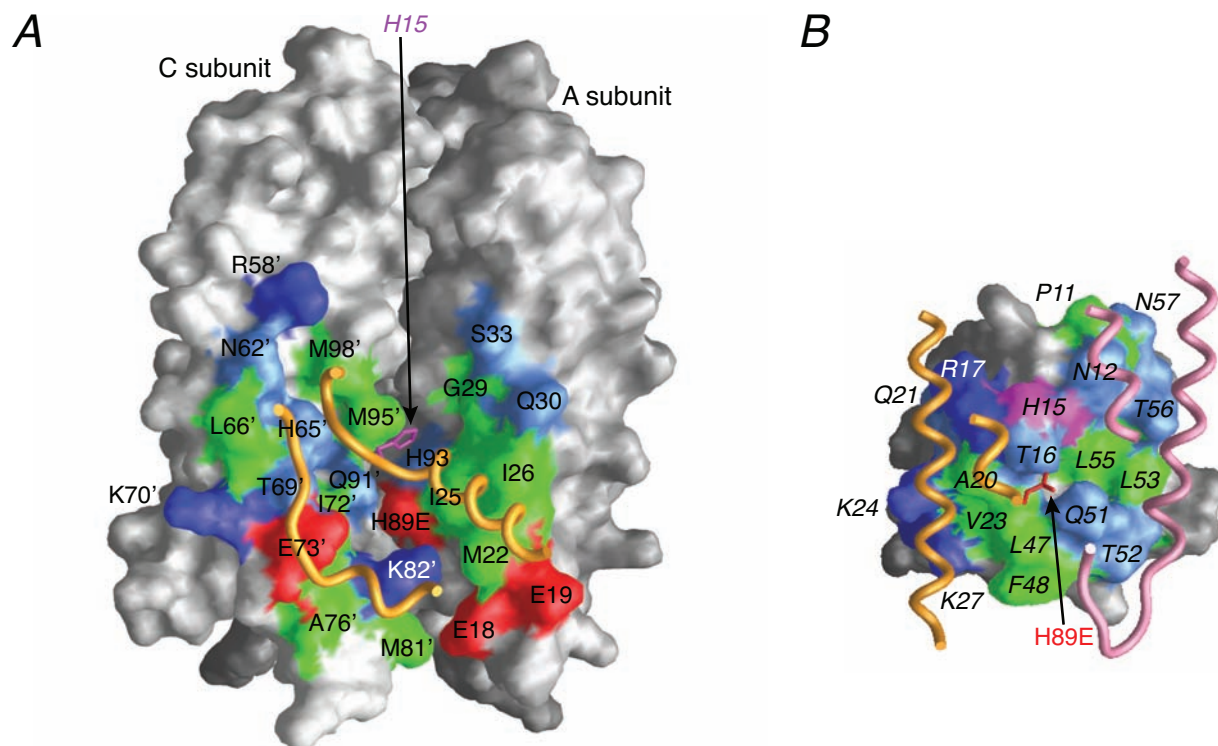
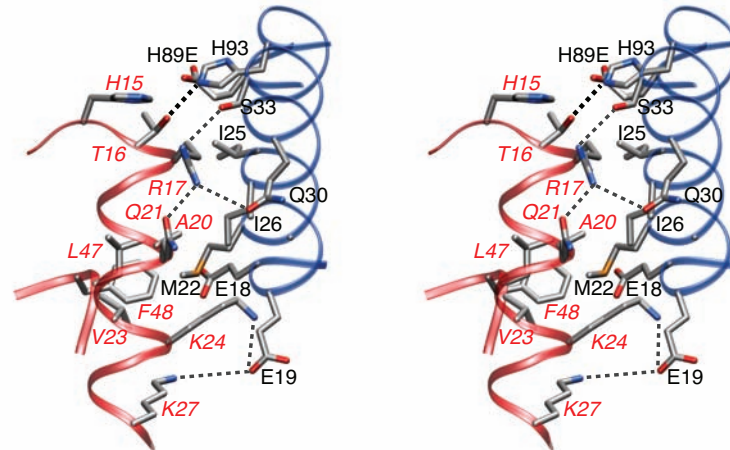
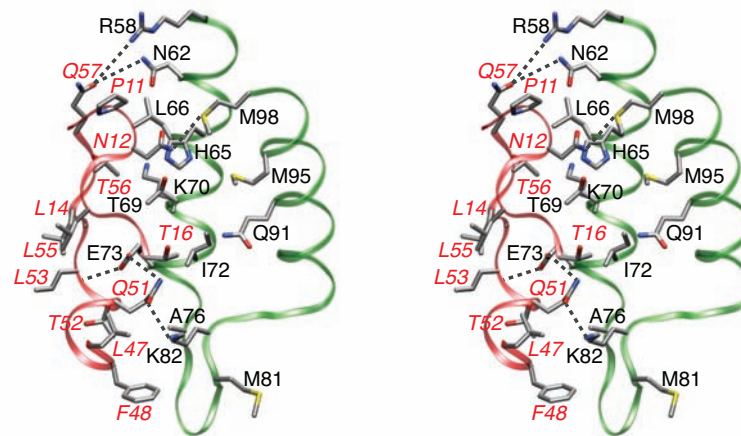


Fig. 4

A



B



C

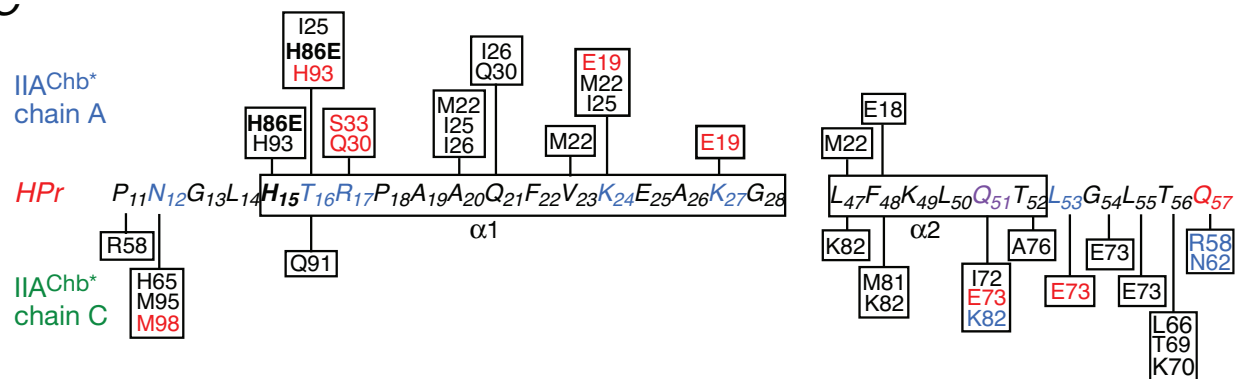


Fig. 5

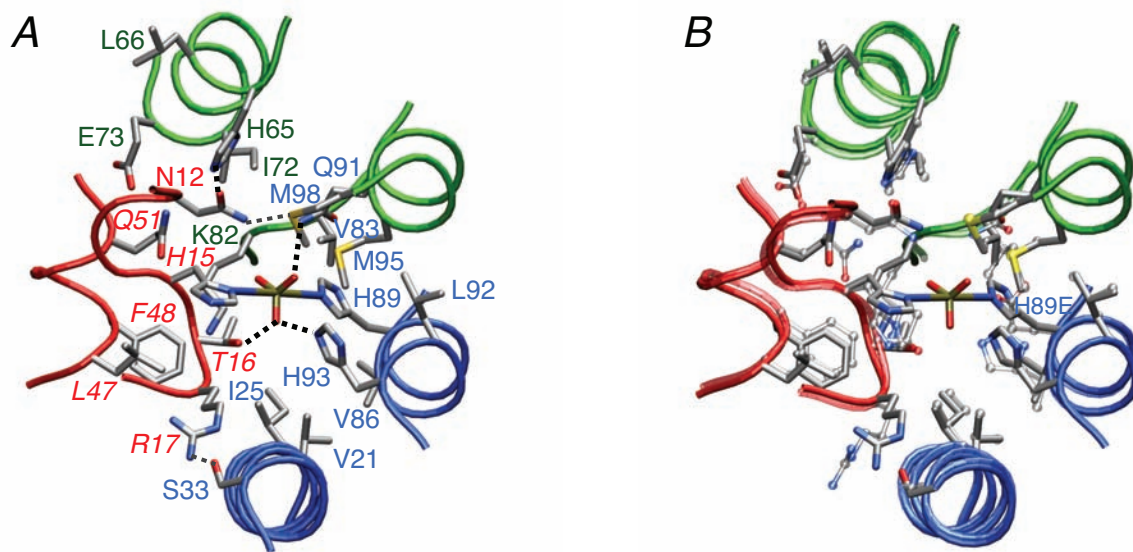


Fig. 6

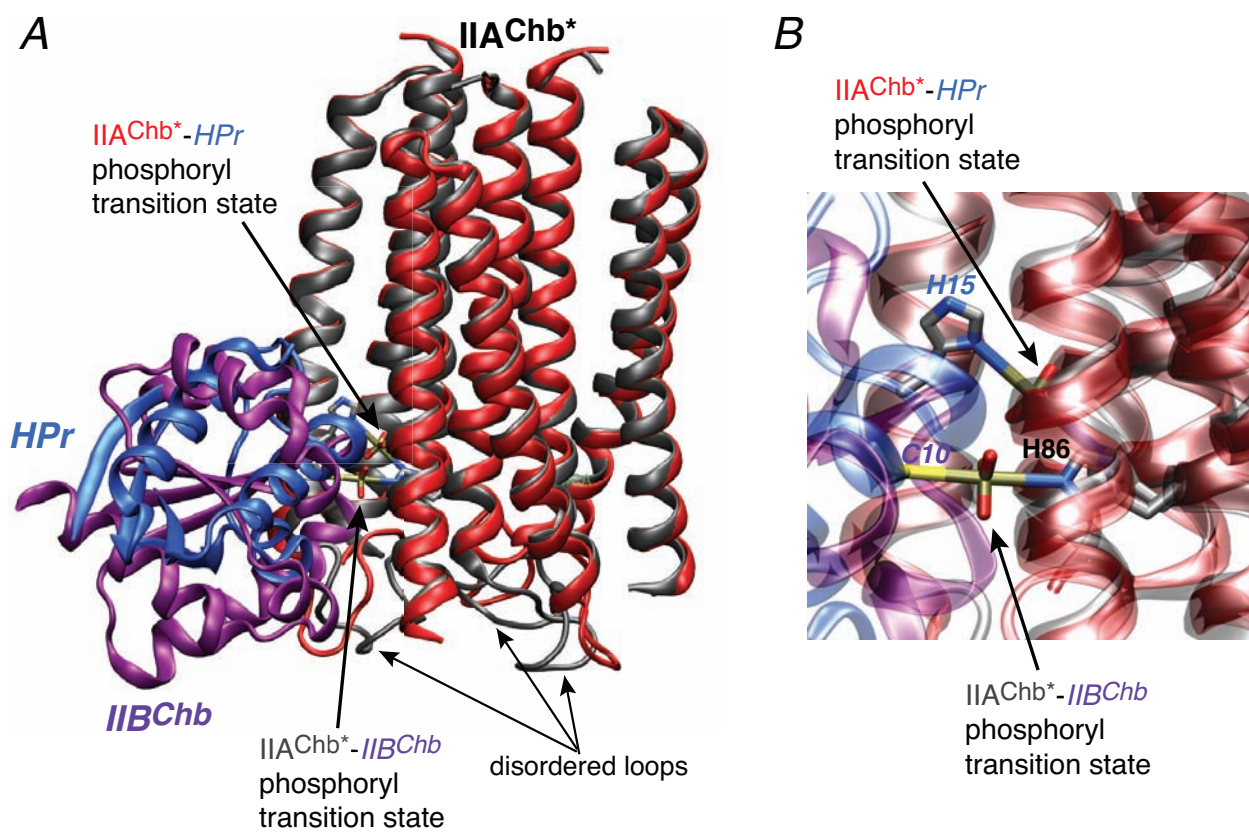


Fig. 7